Lidar Measurements of Wind in the Planetary Boundary Layer: The Method, Accuracy and Results from Joint Measurements with Radiosonde and Kytoon

WILLIAM P. HOOPER* AND EDWIN W. ELORANTA

Department of Meteorology, University of Wisconsin, Madison, WI 58706

(Manuscript received 16 July 1985, in final form 28 December 1985)

ABSTRACT

During the Central Illinois Rainfall Chemistry Experiment (CIRCE), the University of Wisconsin lidar measured wind and turbulence profiles through the planetary boundary layer for a 32-h period in conjunction with surface observations, radiosonde soundings and kytoon profiles made by Argonne National Laboratory. The lidar profiles were made using an advection model for aerosol inhomogeneities as described by Sroga et al.. We discuss improvements to this model and explore the accuracy of the lidar wind and boundary layer depth measurements. In addition, the temporal variation of lidar data was utilized to measure boundary layer depth objectively. Cross sections of the speed, direction and rms variation of the wind for the 32-h period show the daytime convective layer, nocturnal stable layer and transitional periods.

1. Introduction

During the Central Illinois Rainfall Experiment (CIRCE), the University of Wisconsin (UW) scanning lidar made over 80 wind profiles[1] in a 32-h period. The lidar wind measurements coupled with observations made by Argonne National Laboratory (ANL), which include 12 radiosonde soundings, 8 kytoon profiles, and regular half-hour surface observations, provide a detailed picture of the diurnal planetary boundary layer (PBL) wind evolution. The speed, direction and rms variation of the wind were profiled by lidar. The rms variation measures a combination of the turbulence and the mean wind shear in the boundary layer.

Considerable research effort has been devoted to understanding boundary layer dynamics. In part, this effort involves synthesizing wind profiles from field experiments and numerical models. Researchers have used balloons (Clark, 1970), kytoons (Haugen et al., 1975), towers (Kaimal and Gaynor, 1983), and sodars (Kaimal and Haugen, 1977) to provide boundary layer wind profiles. The present search into boundary-layer dynamics demands more information than conventional sensors alone can provide. Scanning lidars can provide additional information about boundary layer motions by observing the movement of aerosol structures. (See Kunkel et al., 1980, Boers et al., 1984, and Sasano et al., 1982a.)

This paper uses the technique described by Sroga et al. (1980) to profile wind parameters through the boundary layer. We also discuss improvements to this model that increase the accuracy of the wind measurements. Lidar data from a triple azimuth angle scan (TAAS) is analyzed to detect the motion of the aerosol structures ranging in size from 100 to 1000 m. As shown in Fig. 1, the TAAS incorporates an almost horizontal scan, where the lidar is fired repetitively at the same elevation angle but alternating between three azimuthal angles separated by 1°. The scans are composed of 400 lidar shots obtained at 1-sec intervals. An actual TAAS is displayed in Fig. 2. The diagonal tracks result from the advection of aerosol structures. This drift of aerosol structure provides signal for measuring the speed, direction and rms variation of the wind.

Observing the boundary layer evolution requires an accurate measure of the PBL depth. Turbulent convective plumes mix the PBL, creating a layer of constant potential temperature observed in the radiosonde soundings. (See Fig. 3.) The temperature jump seen at the top of the layer is commonly used to measure the boundary layer depth. The turbulence also transports aerosols from the surface. The relative differences between the aerosol in the PBL and the clean air above the PBL can also be used to determine the mixed-layer depth (Boers et al., 1984). This change in aerosol loading is readily apparent in the lidar range height indicator (RHI) scan shown in Figs. 4 and 5. The interface separating the boundary layer and the clean air above is normally strongly convoluted. The advection of these

* Present affiliation: Naval Research Laboratory, Washington, DC 20375.

[1] Each profile is formed from individual time- and space-averaged measurements which are vertically spaced from 25 to 100 m apart with this spacing depending on the elevation angle of the lidar scan. The profiles normally start between 50 and 100 m above the surface and end at the PBL top.

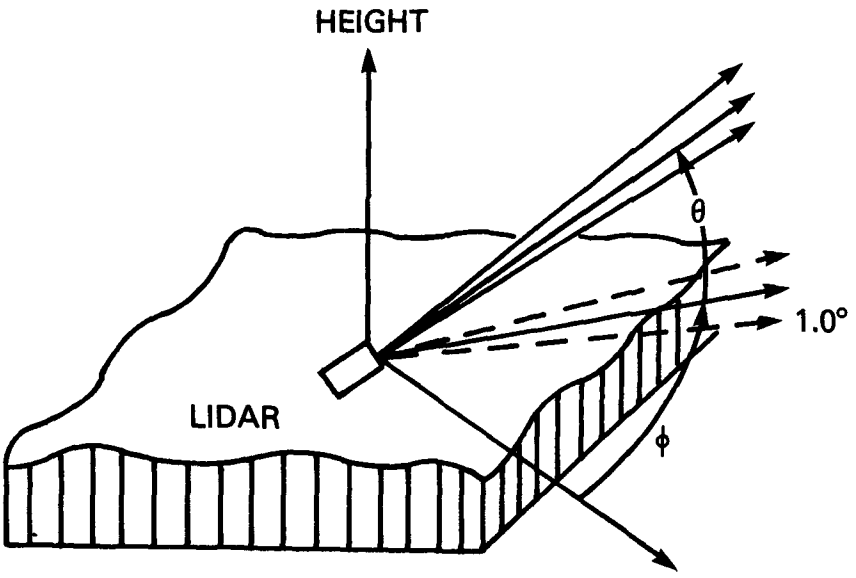

FIG. 1. A TAAS (triple azimuth angle scan). The lidar is fired repetitively at a small, fixed elevation angle (θ) but alternates between three azimuth angles (ϕ) separated by 1°.

convolutions causes a temporal variance in the lidar-observed backscatter. This paper presents a technique which uses the temporal variance in aerosol backscatter to objectively measure boundary layer depths. The boundary layer depths determined with this technique are compared with the depths determined from potential temperature profiles and measured visually by observing the decrease of aerosol loading seen at the top

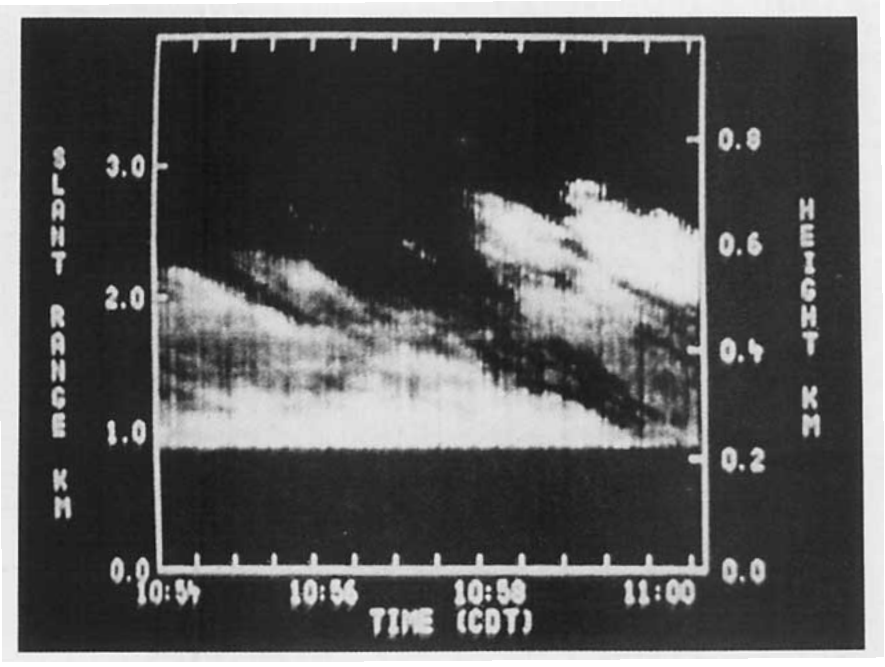

FIG. 2. A TAAS at 12° elevation taken from 1054 to 1101 CDT on 17 July 1979. The scale on the left side is the slant range from the lidar and the scale on the right side is the height above the surface. The attenuation is removed by applying a manually selected, exponentially increasing correction. The light regions represent areas of enhanced backscatter from aerosols carried aloft by convective plumes. The elongation of the structures from upper left to lower right results, in part, from the advection of aerosol structures through the TAAS.

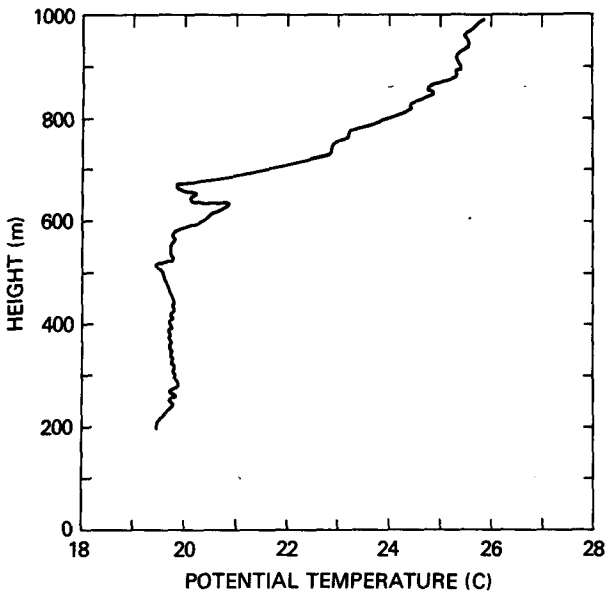

FIG. 3. A radiosonde temperature profile made at 1104 CDT on 17 July 1979 by personnel from Argonne National Laboratory. It was made shortly after the TAAS in Fig. 2. Note that the potential temperature is almost constant from 100 to 700 m.

of the mixed layer in lidar RHI scans. These lidar observations are shown on the wind cross sections.

CIRCE was conducted to study convective storm dynamics and mesoscale precipitation chemistry. A flat agricultural area near Weldon, Illinois (40°07'N, 88°45'W) was used for the experiment. Personnel from ANL made extensive boundary layer measurements using a kytoon and a low-level dual theodolite-tracked radiosonde system described by Frenzen and Prucha (1973). They also obtained surface observations with anemometers, temperature sensors, humidity sensors and a global radiometer. The UW lidar was located 2.6 km southeast of the ANL location, allowing the lidar to make wind measurements above the radiosonde launch site.

2. Analysis techniques

a. Lidar

Lidar measures the power backscattered from a laser beam propagating through the atmosphere. This power return, $P(\phi_i, R_j, t_i)$, for a monostatic lidar pointing at a constant elevation is

$$P(\phi_i, R_j, t_i) = \frac{K\beta(\phi_i, R_j, t_i) \exp[-2\tau(\phi_i, R_j, t_i)]}{R_j^2}, \quad (1)$$

where

t_i = time of the ith lidar profile,
ϕ_i = azimuthal angle for this profile,
R_j = radial distance along the propagation path to the j data point,
K = system constants and laser output energy,
$\beta(\phi_i, R_j, t_i)$ = volume backscatter coefficient, and
$\tau(\phi_i, R_j, t_i)$ = optical depth.

The UW lidar system (see Table 1—Equipment) corrects for energy variation and the inverse-range square decrease in signal:

$$Y(\phi_i, R_j, t_i) = R_j^2 P(\phi_i, R_j, t_i)/E(t_i), \quad (2)$$

where $Y(\phi_i, R_j, t_i)$ is the corrected lidar power return and $E(t_i)$ is the laser output energy. The lidar wind and PBL depth results in this paper are derived from the corrected data.

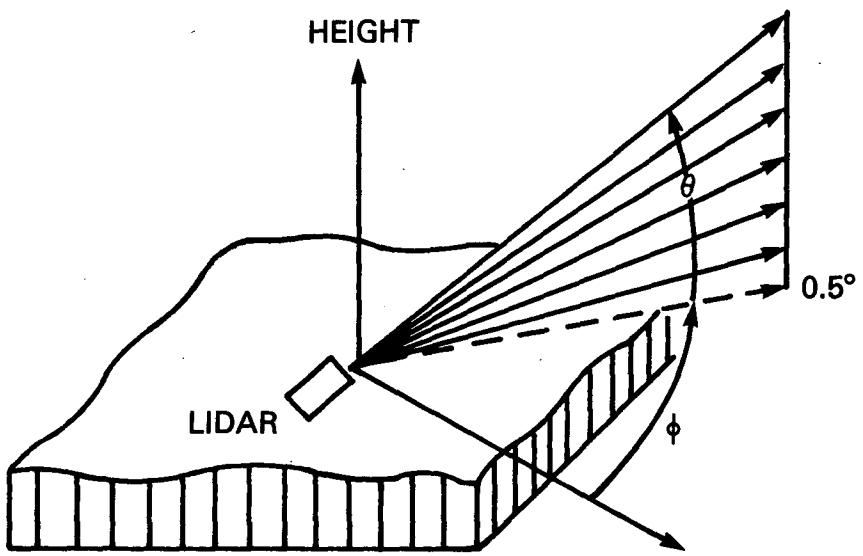

FIG. 4. A RHI scan. The lidar is fired at a fixed azimuthal angle, but the elevation angle is incremented through every half-degree between 2° and 24°.

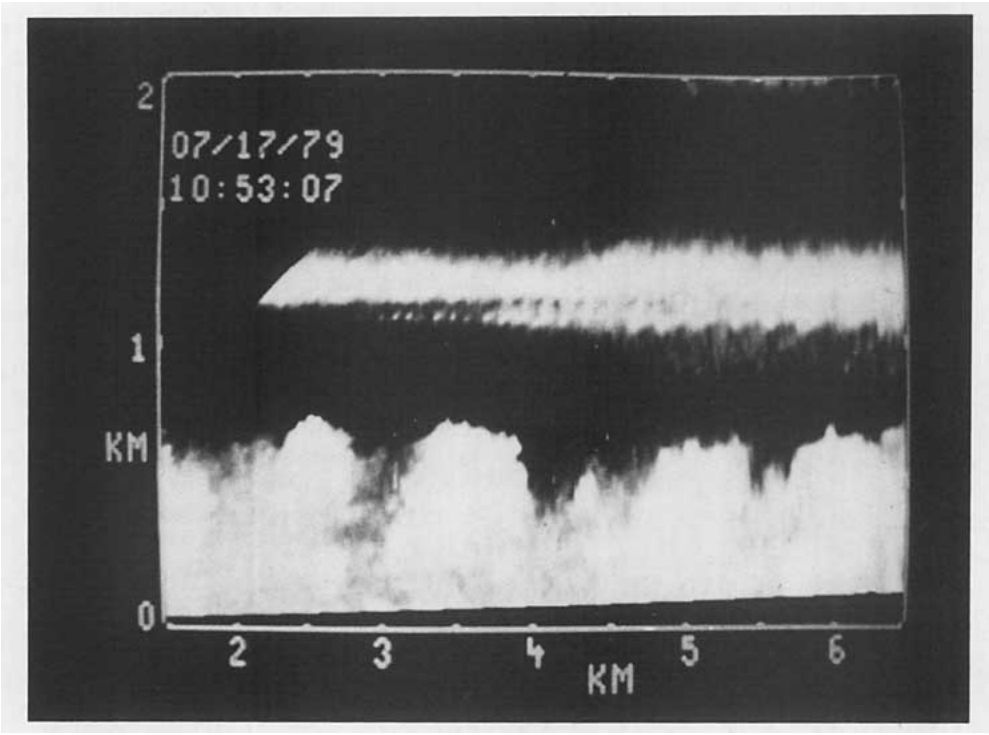

FIG. 5. Display of the RHI scan at 1053 CDT 17 July. The optical attenuation is removed by applying a manually selected, exponentially increasing correction. The light regions below 1 km represent areas of enhanced backscatter from aerosols carried aloft by rising convective plumes. The light region above 1 km is a stable layer above the boundary layer.

b. PBL height

As discussed in the Introduction, a large gradient of backscatter marks the top of the boundary layer. Boers et al. (1984) used the gradient in RHI scans to determine the boundary layer depth. The variability of lidar return observed in the center shots of a TAAS also provides a measure of PBL depth. The advection of the convoluted interface at the boundary layer top through a series of lidar shots pointed in the same direction produces this temporal variability. This variability decreases below the PBL top, where the contrast between aerosol structures are small, and above the PBL top, where the air is clear. Thus the height of the maximum variance objectively determines the PBL depth.

We estimate the backscatter variance from the corrected lidar returns. The power return for one range from each center shot in a TAAS forms a time series. The time series are analyzed for the mean, $\bar{Y}^i(\phi_2, R_j)$, and covariance, $\overline{Y'^2}^i(\phi_2, R_j)$:

$$\bar{Y}^i(\phi_2, R_j) = \frac{1}{N-1} \sum_{i=1}^{N-1} Y(\phi_2, R_j, t_i), \tag{3}$$

$$\overline{Y'^2}^i(\phi_2, R_j) = -\frac{1}{N-1} \sum_{i=1}^{N-1} [Y(\phi_2, R_j, t_i) - \bar{Y}^i(\phi_2, R_j)][Y(\phi_2, R_j, t_{i+1}) - \bar{Y}^{i+1}(\phi_2, R_j)], \tag{4}$$

where N is the total number of center shots in the TAAS and ϕ_2 is the center azimuthal angle of the TAAS. The covariance is computed for lidar shots separated in time (by $\sim$2 sec) rather than the variance because this small time separation effectively removes noise that is not correlated between lidar shots. At the small time separations, we expect the covariance to approximate the variance. A normalized backscatter variance, $W(\phi_2, R_j)$, is approximated by dividing the covariance of the power return by the mean power return. This normalization removes the mean attenuation:

$$W(\phi_2, R_j) = \frac{\overline{Y'^2}^{i+1}(\phi_2, R_j)}{\bar{Y}^i(\phi_2, R_j)\bar{Y}^{i+1}(\phi_2, R_j)}. \tag{5}$$

The normalized covariance results from variability of backscatter and optical thickness. This is seen by expanding the optical thickness expressed in Eq. (1) into a power series. After third and higher-order terms are neglected, the normalized power return variance is approximated by three terms:

$$W(\phi_2, R_j) \cong \underbrace{\frac{\overline{\beta'^2}^i(\phi_2, R_j)}{[\bar{\beta}^i(\phi_2, R_j)]^2}}_{\text{(i)}} + \underbrace{\frac{\overline{4\beta'(\phi_2, R_j)\tau'}^i(\phi_2, R_j)}{\bar{\beta}^i(\phi_2, R_j)}}_{\text{(ii)}} + \underbrace{\overline{4\tau'^2}^i(\phi_2, R_j)}_{\text{(iii)}}. \tag{6}$$

TABLE 1. University of Wisconsin lidar systemparameters (1979).

Transmitter	
Wavelength	694.3 nm (ruby)
Output Energy	1.0–1.5 J/pulse
Pulse Duration	20 ns
Beam Divergence	1 mrad
Receiver	
Telescope	0.31 m Newtonian
Field of view	Adjustable (1.5–7 mrad)
Detector	RCA 70042K PMT
Quantum Efficiency	6.8% at 694.3 nm
Spectral Bandpass	1.0 nm (Interference filter)
Mount Positioning	
Elevation/Resolution	0.0–50.0/(0.1)
Azimuth/Resolution	0.0–70.0/(0.1)
Data Logging	
Amplifier	Logarithmic (80 db)
Digitization	Biomation 1010 (10 bit)
Range Resolution	15 m
Preprocessor	PDP 11/40 Minicomputer
Color Display	
Output	Color Monitor 21 inch diagonal
Screen Resolution	512 lines, 620 dots/line
Color Scales	3 selectable colors, 32 intensity levels/color

These terms are

(i) the normalized backscatter variance,
(ii) the covariance of the backscatter and optical thickness, and
(iii) the variance of the optical thickness.

When the variable component of the optical thickness is small, the normalized covariance is dominated by the backscatter variance and the peak normalized covariance occurs at the PBL top. The profile shown in Fig. 6 is close in time to the RHI scan (Fig. 5) and potential temperature profile (Fig. 3). If the top of the boundary layer is marked by a sharp change in backscatter, and variance is caused by the movement of this boundary up and down, the magnitude of the variance is proportional to the backscatter cross-section variation across the boundary and is dependent on the percentage of time the boundary spends above and below that height. We compared lidar PBL depth measurements made from normalized variance and RHI scans with the depth of mixed layer in radiosonde temperature profiles. To minimize errors caused by the time separation between lidar and radiosonde observations, the lidar observations before and after a radiosonde profile were interpolated to the time of the radiosonde profile. The interpolations were done independently for heights derived from normalized variance profiles and from RHI scans. Both types of lidar measurements had a 99% correlation with the radiosonde profiles. The comparisons included 16 variance profiles and 16 RHI scans with the boundary layer depth ranging from 150 to 1300 m. During the 32-h period mentioned in the Introduction, 134 lidar PBL depth measurements were made. These measurements are presented in the cross sections discussed in section 3.

c. *Wind measurement*

The speed, direction and rms variation of the wind are determined from the movement of the aerosol inhomogeneities through a TAAS. Sroga et al. (1980) filter lidar data to generate aerosol inhomogeneity profiles. These profiles, starting at ranges greater than 1000 m, are separated into segments of either 500 or 1000 m in length. Since the angular separation between beams is 1° or 2°, the segments are almost parallel. These segments provide a measure of the change in aerosol structures over a range of temporal and spatial separations. The segments are Fourier transformed from ranges R_a to R_b:

$$F(k, \phi_i, t_i) = \sum_{j=a}^{b} \tilde{Y}(\phi_i, R_j, t_i) \exp(-2\pi ikR_j), \quad (7)$$

where k is the wavenumber and $\tilde{Y}(\phi_i, R_j, t_i)$ is a lidar segment that is filtered and cosine tapered. Fourier transforming the data reduces the computational time and allows results from different wavenumbers to be optimally filtered. The segments are cosine tapered to minimize biasing of the Fourier components. Modeling the cross spectral phase shift (CSPS) and coherence between segments determines the wind parameters over the height range of the segments. By using the segments at different heights, profiles of the wind speed, direction and rms variation are measured.

The CSPS and coherence are calculated from the smoothed cross spectrum, $\tilde{S}(k, \phi_i, \phi_{i+m}, \Delta t)$:

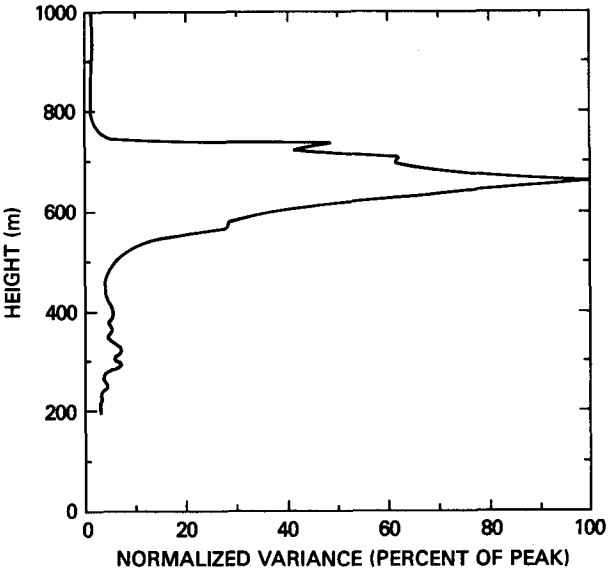

FIG. 6. Profile of the normalized backscatter variance from the TAAS shown in Fig. 2.

$$\tilde{S}(k, \phi_i, \phi_{i+m}, \Delta t) = \frac{1}{N}\sum_{m=1}^{N} F(k, \phi_i, t_i)F^*(k, \phi_{i+m}, t_{i+m}), \quad (8)$$

where

m = number of lidar returns separating the two segments,
Δt = time between lidar measurements (m time separations between shots),
ϕ_i and ϕ_{i+m} = azimuthal angles for which the cross spectrum are calculated,
N = number of segments in each time series, and
$*$ denotes the complex conjugate.

The weighted coherence is calculated from the smoothed spectrum:

$$\mathrm{coh}(\Delta x, \Delta t) = \sum_{k=1}^{M} W(k)\frac{\tilde{S}^*(k, \phi_i, \phi_{i+m}, \Delta t)\tilde{S}(k, \phi_i, \phi_{i+m}, \Delta t)}{\tilde{S}(k, \phi_i, \phi_i, 0)\tilde{S}(k, \phi_{i+m}, \phi_{i+m}, 0)}, \quad (9)$$

where Δx is the time-averaged lateral separation between the time series of lidar segments:

$$\Delta x = |\sin(\phi_i - \phi_{i+m})(R_a + R_b)/2|, \quad (10)$$

M is the total number of wavenumbers, and $W(k)$ is the normalized weight of the kth wavenumber generated by an optimal filter from Sroga (1979). For measuring winds, the cross spectral phase shift and coherence of these aerosol structures are calculated for 3 spatial separations and 96 TAAS temporal separations between +46 and −46 sec. The three spatial separations include zero separation for shots in the same direction and separations of approximately 100 and 200 m for the shots in different directions; the exact separation depends on the average range of the segment.

The wind affects shape and location of the CSPS and coherence. The time separation of the peak coherence approximately equals the time required for aerosol structures to drift between parallel but separated segments, thus determining the lateral wind speed. The CSPS at the time of the peak coherence measures the radial displacement of the aerosol structures along the lidar beam, providing a measure of the radial wind speed. The model of the average radial wind speed, v, includes the cross spectra phase shift, $\Delta\psi(k)$, and the angle, α, between the lidar beam and the peak correlation axis:

$$v = \sum_{k=1}^{M} W(k)\left[\frac{\Delta\psi(k)}{2\pi k\Delta t} + \left(\frac{\Delta x}{\Delta t} - u\right)\tan\alpha\right]\sin\theta, \quad (11)$$

where u is the average radial wind speed and θ is the elevation angle of the TAAS. Sasano et al. (1982b) clearly demonstrate that the aerosol structures in the boundary layer are anisotropic. Sroga et al. (1980) use the first term in the above equation to measure winds for isotropic aerosol structure. We added the second term to correct for the anisotropic shape effects. If the aerosol structures are elongated, the aerosol structure may have a peak correlation axis which is, in general, aligned with neither the wind nor the lidar beam. The angle between the peak correlation axis and the lidar beam is assumed to be constant, despite the small time dependence caused by the turbulence decay of the aerosol structures. The phase shift results from the radial wind velocity ($v\Delta t$) and the peak correlation axis [$(\Delta x - u\Delta t)\tan\alpha$].

The second term in Eq. (11) corrects for apparent radial motion of an asymmetric aerosol structure when it is observed along two lines of sight separated laterally by a Δx. Figure 7 shows the CSPS observations from the largest wavenumbers for one wind measurement and the model fit to these data. The lines represent the fit of all phase measurements for that wavenumber. If the second term in Eq. (11) were zero, all the phase shift observations would fall on the dashed line, but instead, the different separations fall on different lines. The CSPS with the correction term enables the use of phase measurements at more time delays than the uncorrected equation; therefore, the corrected model is expected to have a smaller random measurement error. We calculated the radial wind with and without the anisotropic correction term. The rms differences of the radiosonde measurements compared to the corrected and uncorrected radial wind are 0.5 and 1.8 m s^{-1}, respectively.

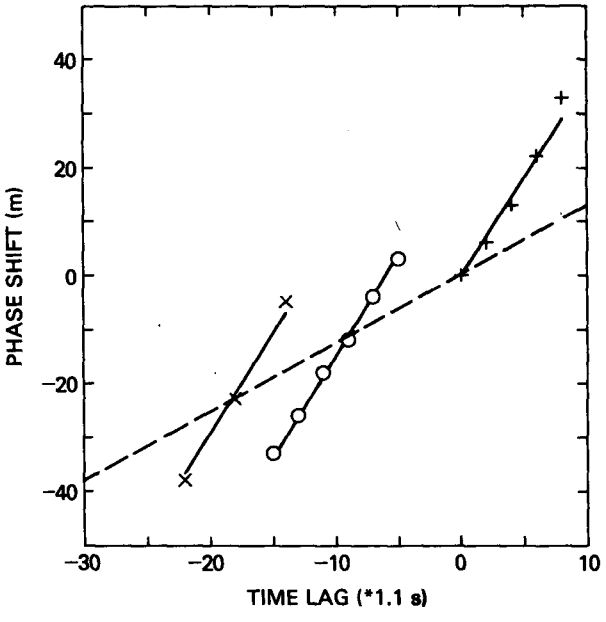

FIG. 7. Cross-spectral phase shift observed in one radial wind speed measurement. The ordinate is the phase shift scaled to be the distance the aerosol structures drift radially along the lidar beams. The abscissa is the time lag between the lidar segments. Shown is the observed phase shift for 0 m (plus), 59 m (zero) and 118 m (cross) separation between lidar segments. The phase shift caused by the radial wind alone is shown by the dashed line. The solid lines are determined from a least-squares fit to Eq. (10).

Sroga (1979) derives a model for the advection of a Gaussian and homogeneous aerosol distribution. This model contains an isotropic Gaussian velocity spectrum. The predicted coherence of this aerosol structure is

$$\mathrm{coh}(\Delta x, \Delta t) = A\left(\frac{2\sigma_a^2}{2\sigma_a^2 + \sigma_s^2\Delta t}\right)\exp\left[\frac{-(\Delta x - u\Delta t)^2}{2\sigma_a^2 + \sigma_s^2\Delta t^2}\right] \times \left[\sum_{i=1}^{M} W(k)\exp(-4\pi^2k^2\sigma_s^2\Delta t^2)\right], \quad (12)$$

where A is the amplitude, σ_a the rms width of the aerosol inhomogeneities, and σ_s the rms variation of the wind. The peak coherence occurs at a time separation slightly smaller than the average time separation necessary for the aerosol structures to drift between the lidar beams. This time shift depends on the rms variation of the wind. In order to derive both the cross path velocity, u, and the rms variation of the wind, σ_s, a nonlinear regression procedure is used to provide a best fit of Eq. (11) to the measured coherence data. This regression provides an amplitude, A, and a mean structure size, σ_a, as well as the values of u and σ_s.

The wind speed, V, and direction, ϕ, are calculated from lidar measured radial and lateral wind speed:

$$V = (u^2 + v^2)^{1/2} \quad (13)$$

and

$$\phi = \tan^{-1}(u/v) + \bar{\phi} + 180°, \quad (14)$$

where $\bar{\phi}$ is the average direction of the TAAS.

The lidar, radiosonde and kytoon observations represent different measurements of a turbulent wind field. Lidar winds are averaged in time by the temporal length of the TAAS and in space by the area outlined by the lidar data segments; in contrast, the radiosonde and kytoon average the winds along the balloon trajectory. This effect, coupled with atmospheric variability, induces differences in the wind observations not caused by instrumental errors. We minimize these differences by averaging the radiosonde and kytoon observations over the vertical extent of the lidar measurements and comparing observation pairs separated by less than 10 min. (See Figs. 8a, b.) The lidar and radiosonde measurements are similar in the daytime convective layer. The comparison of lidar and kytoon measurements shows that lidar can measure winds in the nocturnal stable boundary layer and during the transition periods between the stable and convective layers.

Boers et al. (1984) optimize the vertical turbulence scaling velocity:

$$\sigma_w^3 = w_*^3 + \frac{A_s}{A_f}u_*^3, \quad (15)$$

where w_* is the convective velocity, u_* the fraction velocity, and A_s and A_f are constants. We assume that this scaling velocity is proportional to the turbulence in the boundary layer. The optimal values of A_s and A_f are found by Boers et al. (1984) to be 7.5 and 0.32, respectively. The convective velocity scale, w_*, is calculated from the surface virtual potential temperature flux, Q_0, and PBL depth, Z_i:

$$w_* = \left(\frac{gQ_0Z_i}{T}\right)^{1/3}, \quad (16)$$

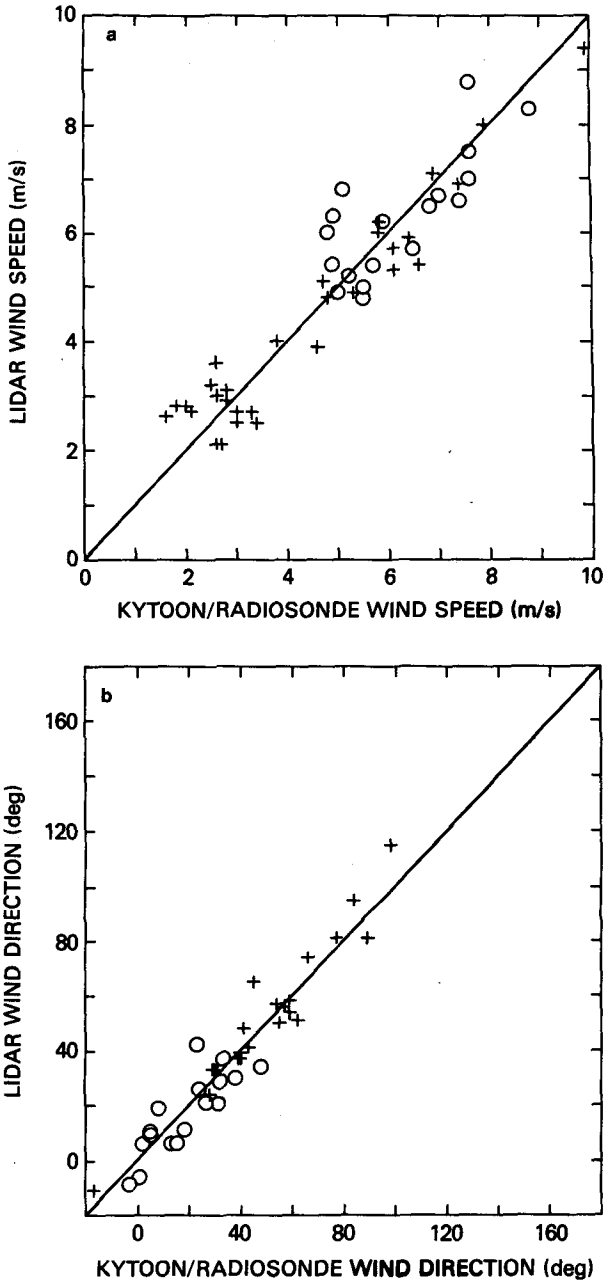

FIG. 8. Lidar (a) wind speed and (b) direction compared with radiosonde and kytoon measurements. The radiosonde (WHATS) and kytoon comparisons are denoted by (zero) and (plus), respectively. The WHATS observations were taken during the daylight hours, and the kytoon data were primarily taken during evening and early morning hours. The measurements compared are within 10 min of each other and averaged over the vertical depth of lidar observation.

where g is the gravitational acceleration and T the surface temperature.

Lidar measurements of the PBL depth are used and combined with surface potential temperature flux. This flux is calculated from measurements of the sensible heat flux, H, and latent heat flux, H_l, made by personnel from Argonne National Laboratory:

$$Q_0 = H + 0.61 C_p T \frac{H_l}{L_e}, \tag{17}$$

where C_p is the specific heat of air at constant pressure and L_e is the latent heat of condensation.

The rms variation of the wind measures the decrease in coherence between lidar segments with increasing temporal separation. Both convective turbulence and wind shear cause this decrease in coherence. Convective turbulence advects different aerosol structures at different velocities, and wind shear changes the shape of aerosol structures in time. To determine the relative importance of turbulence and wind shear on the rms variation, we used a simple empirical model:

$$\sigma_m = (A\Delta V^2 + B\sigma_s^2)^{1/2}, \tag{18}$$

where σ_m is the modeled rms variation of the wind, ΔV is the magnitude of vector difference between wind at the top and bottom of the lidar range interval, and A and B are constants. The squared magnitude of rms variation, wind shear and scaling velocity for vertical turbulence were averaged over half-hour intervals. The parameters for wind shear (A) and scaling velocity for vertical turbulence (B) were found from least-squares fitting of the daytime data to be 0.06 and 0.30, respectively. The correlation coefficient between model and measured rms variation is 0.94. Therefore, wind shear has only a small effect on the daytime measurement of rms variation.

During the night, however, the influence of wind shear is considerably stronger. We computed hourly averages of the rms variation and wind shear. The correlation between these parameters for the nine hours of observation is 0.85. The wind variance to wind shear ratio ($\sigma_s/\Delta V$), determined from least squares, is 0.35. In the small data sample analyzed, we could find no evidence that the angle between the lidar segment and wind shear affected the rms variation.

3. Observational results

The UW scanning lidar observed the boundary layer over flat farmland almost continuously for 32 h. During this period, a high pressure system dominated the circulation over the lidar site. As shown by Table 2, the geostrophic wind decreased from 11 to 3 m s^{-1} and veered northeasterly as the high drifted eastward.

Time–height cross sections of the wind parameters were used to visualize the boundary layer evolution. The wind speed and direction cross sections in Figs. 9a and b are formed from kytoon, radiosonde and lidar data. Fig. 9c shows the cross section for the lidar-observed rms variation of the wind. Figs. 9a, b and c represent the cross sections for 17 July; Figs. 10a, b and c are the continuation of these figures for 18 July. The boundary-layer top, marked on cross sections, represents a smoothing spline fit to all lidar measurements not affected by clouds. In discussing these cross sections, we arbitrarily divide the cycle into five PBL periods: evening formation, nocturnal evolution of the stable shear layer, morning transition from the stable to convective layer, morning growth of the convective layer, and afternoon transition from the convective to stable layer.

TABLE 2. Geostrophic winds.

Time (CST)	Speed (m s^{-1})	Direction (deg)
	17 July	
0800	10.3	46.6
0900	10.9	42.5
1000	11.0	44.3
1100	11.8	45.9
1200	11.4	47.8
1300	11.0	47.9
1400	12.4	49.0
1500	11.7	47.9
1600	10.7	49.8
1700	11.0	52.0
1800	9.0	52.2
1900	9.5	53.6
2000	9.5	50.4
2100	9.4	52.7
2200	8.1	53.8
2300	7.0	56.4
2400	6.9	47.8
	18 July	
0100	7.0	49.6
0200	6.9	46.6
0300	7.5	46.4
0400	7.6	49.0
0500	7.3	46.6
0600	6.0	46.1
0700	5.8	45.1
0800	5.1	46.9
0900	8.0	61.6
1000	4.4	45.9
1100	3.7	43.6
1200	3.3	43.7
1300	3.3	47.7
1400	2.4	52.0
1500	3.8	57.1
1600	3.3	67.4

a. Evening formation

As discussed by Caughey et al. (1979), a "transition" occurs in the evening "between onset of negative heat flux and cessation of turbulence near the surface." The surface cools and the air above the surface layer accelerates under the influence of local pressure gradients and topography. On 17 July, the beginning of transition occurs at 1915 CDT and almost coincides with the

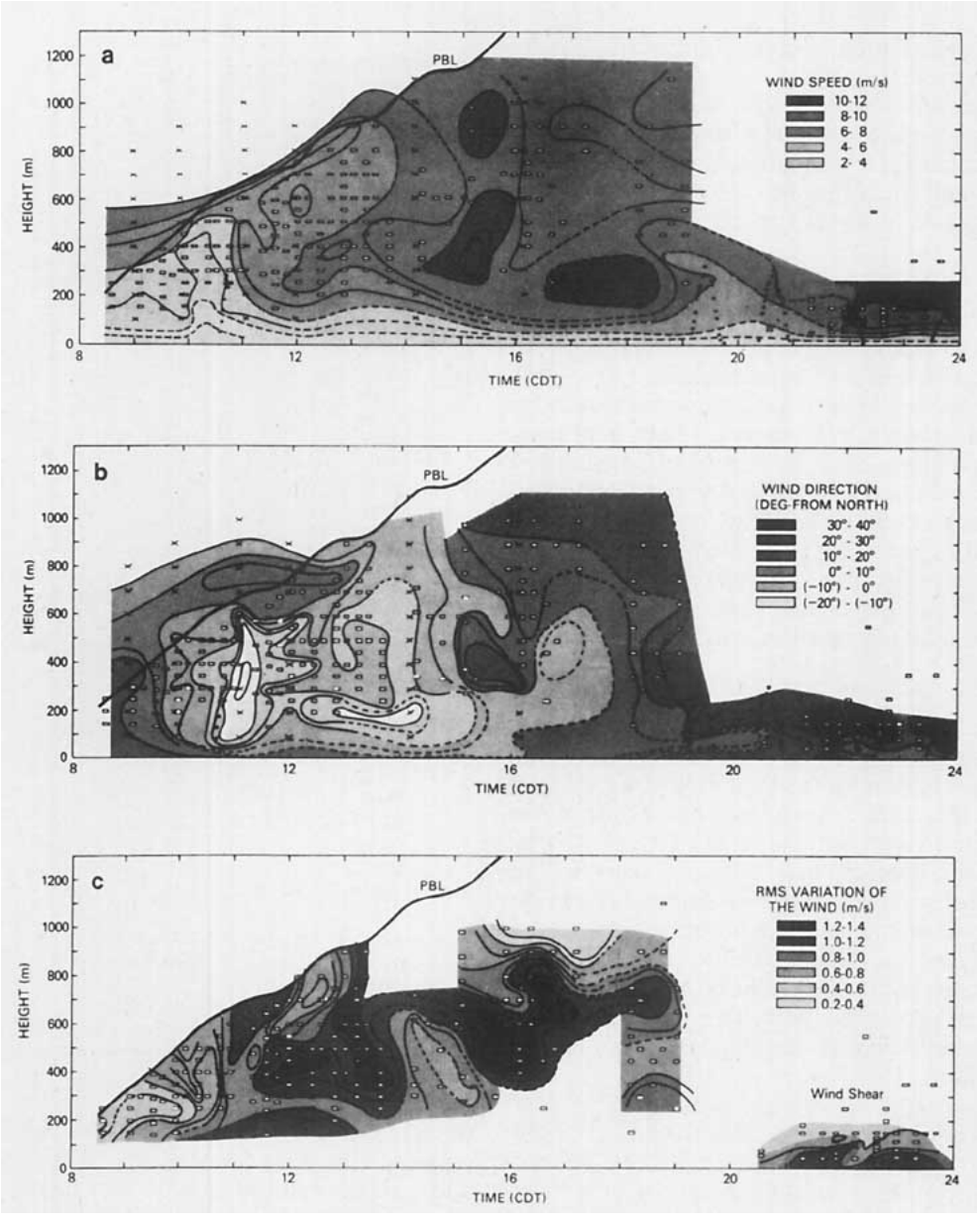

FIG. 9. Time-height (rectangle) × cross sections (circle) for (a) speed, (b) direction and (c) rms variation of the wind formed from lidar, radiosonde, kytoon and surface data on 17 July. The heavy solid line represents the top of the convective boundary layer. The radiosonde, kytoon and surface data were provided by Argonne National Laboratory.

development of a directional wind shear through the surface layer. Lidar wind measurements are made at 15-min intervals between 2130 and 2345 CDT on this date. The surface cooling forms a thin haze layer near the surface. The contrast between the haze at the surface and clear air above provides the backscatter structure which allows lidar wind measurements. Triple azimuth angle scans are taken at 3° and 6° with vertical resolutions of 25 and 50 m, respectively. The cross sections reveal a surface layer with strong speed and directional shear. The shear changes rapidly with possible "bursting" (Businger, 1973) occurring at about 2200 CDT. The large rms variation of the wind is caused by wind shear, not by turbulence.

b. Nocturnal evolution of the stable shear layer

After midnight, RHI scans show a surface haze layer with little apparent structure. Between midnight and early morning, the lidar wind profiles are similar. Beginning at 0400 CDT, turbulent structures reappear in the lidar RHI scans. The contrast between the haze in the boundary layer and the clear air above continues to provide good signal for the lidar wind profiles. The

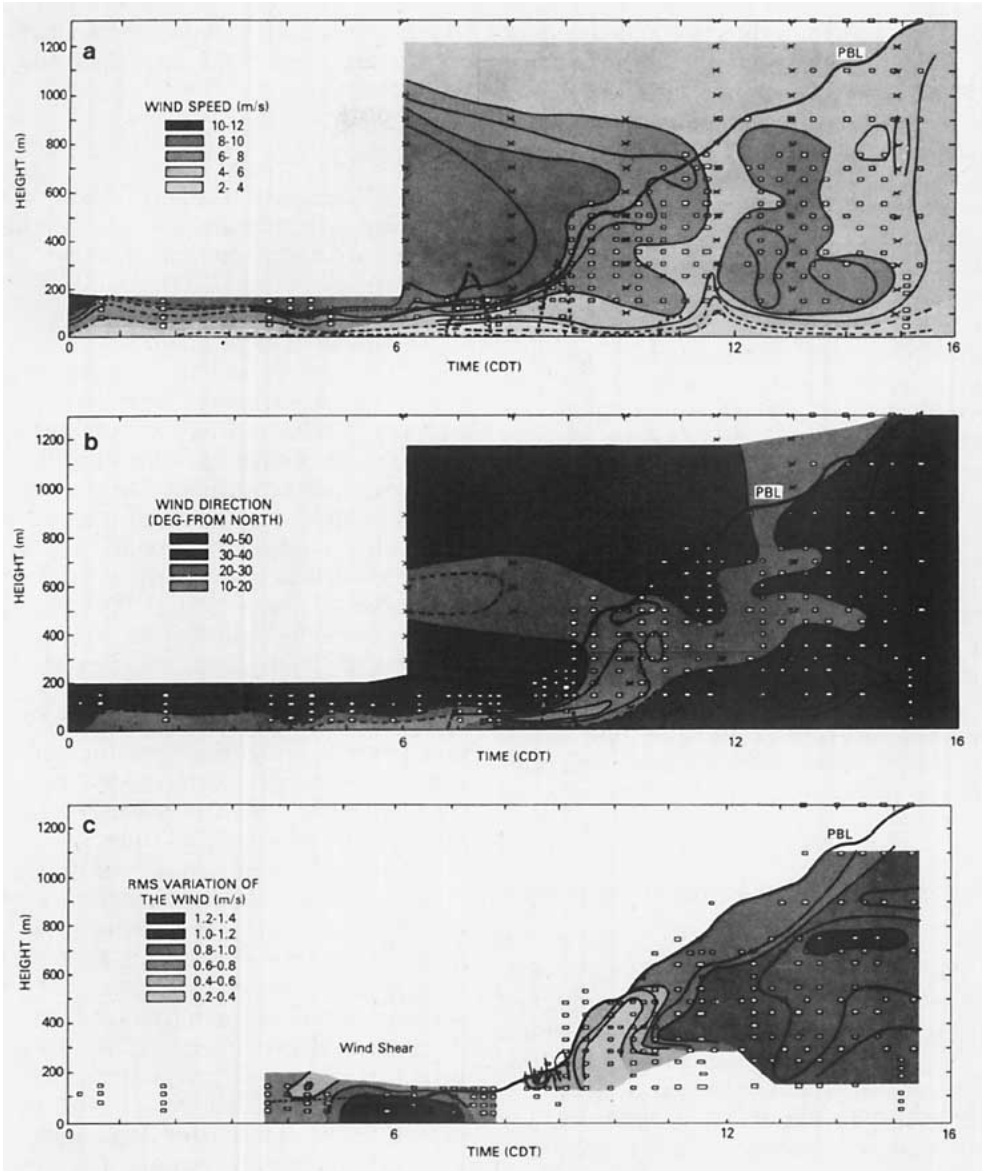

FIG. 10a–c. As in Figs. 9a, b and c, respectively, for continuation into 18 July.

profiles reveal increased shear in the layer. The strength of speed and directional shear varies considerably during the early morning. The slower variations indicate a boundary layer modulated by external forcing, but the source of the forcing is uncertain.

c. *Morning transition from the stable to convective layer*

After 0600 CDT on 18 July, the boundary layer evolves from a stable shear-driven layer to a convective layer. The RHI scans show plumes in the "clear" convective boundary layer growing through the haze layer. The convective layer removes the nocturnal wind maximum, and the wind shear in the surface layer decreases. However, a thin layer sandwiched between the nocturnal wind maximum and the surface layer maintains its wind direction until almost 1000 CDT.

Since the rms variation measures both the wind shear and the convective turbulence, the rms variation cross section reflects the gradual decrease in wind shear and increase in convection. The rms variation decreases with the decreasing wind shear, reaches a minimum at 1000 CDT, and increases with the increasing convective turbulence.

d. *Morning growth of the convective layer*

The rapidly growing convective boundary layer carries aerosols aloft, providing a strong contrast between the aerosol in the plumes and the clear air entrained from above the boundary layer. The wind profiles are made with TAAS (6° and 12° elevation) at 15-min intervals; a comparison of lidar derived winds with kytoon and radiosonde winds shows wind speed differ-

ences of 0.5 m s^{-1} and wind direction differences of less than 5°. The cross sections reveal a well-defined PBL top measured by both RHI and TAAS. The 6° TAAS's provide a vertical resolution of 50 m, more than the 100 m resolution of the 12° TAAS's; but while the 6° TAAS's only reach 750 m, the 12° TAAS's reach 1500 m. Thus the 12° TAAS's are important in the late morning after the PBL grows above 750 m.

The growth of the morning convective boundary layer is highly variable, depending, in part, on the temperature and wind structure above the layer. The cross sections resolve the considerable detail of both the boundary layer depth, marked by the solid line, and the interfacial zone between the boundary layer and the air above. For example, at 0900 CDT on 18 July, the boundary layer grows rapidly, the wind speed in the entrained air decreases, and a thin layer with wind shear at the top of the boundary layer is maintained.

Variations of heating and advection also influence the growth and evolution of the convective boundary layer. The 15-min temporal resolution in the cross sections allows the observations of short-term variation not always apparent in hourly radiosonde data. The rapid wind shift that occurs on 17 July at 1045 CDT might fall between soundings; fortunately, this shift is observed by kytoon, radiosonde and lidar. This shift coincides with an increase in speed and rms variation of the wind.

e. Afternoon transition from the convective to the stable layer

The late afternoon presents a difficult wind observation period for the lidar. The structures are larger than morning structures, and the aerosol in the boundary layer is well mixed with reduced contrast between PBL structures and structures entrained earlier in the day. These problems are minimized by increasing the lidar segment used in wind observations from 500 to 1000 m. While the information content of the segment increases and larger PBL structures are observed, the vertical resolution decreases from 100 m for a 12° TAAS to 200 m. Even with longer segments, the signal-to-noise ratio is occasionally too small and wind measurements cannot be made.

On 17 and 18 July, lidar wind observations through the daytime boundary layer are made until 1900 and 1530 CDT, respectively. In the early afternoon of 18 July, the winds in the boundary layer are almost constant. As the solar heating decreases, the surface influence decreases, resulting in wind shear and convective turbulence being stratified to thin layers. These stratifications, while not apparent in the speed and direction cross sections for 18 July, appear in the cross sections of the rms variation. Similarly, on 17 July, horizontal stratifications appear in wind speed and rms variation cross sections. During the late afternoon, the rms variation indicates a decreasing convective turbulence and increasing wind shear. The transition from a convective to stable boundary layer, while less dramatic than the reverse transition in the morning, is observed in the lidar data.

4. Summary

The UW scanning lidar observations, during CIRCE, combined with radiosonde and kytoon measurements provide a detailed picture of the evolution of the boundary layer for a 32-h period.[2] Both the depth and the winds in the boundary layer were accurately measured by lidar. The normalized variance provided an objective measure of the boundary layer depth. A comparison of the mixed-layer depth observed in radiosonde profiles and depths found using the normalized variance profiles agreed within 50 m. Most of the differences can be attributed to the sample errors involved in measuring the depth of a convoluted mixed layer with a single radiosonde. These observations coupled with lidar observations of the depth made from RHI scans by Boers et al. (1984) provided high, 15-min temporal resolution of the boundary layer depth, allowing the layer growth between hourly radiosonde profiles to be monitored. Additional work is needed to completely understand the normalized variance profiles. The peak of the normalized variance profile occurs near the boundary layer top; in addition, the depth for the "half-width" of this peak may be comparable to the depth of the interfacial zone.

We used an improved version of the Sroga et al. (1980) model to measure wind profiles. We found that this technique could measure wind speed and direction in the daytime convective layer, nocturnal stable layer, and transition layers in between. The lidar-derived wind speed and direction compared favorably with radiosonde and kytoon profiles with accuracies better than 1 m s^{-1} and 10°, respectively. The lidar profiles were frequently made every 15 min and provided details of the boundary layer development between the hourly radiosonde observations. The lidar observed rms variation of the winds provides a measure of turbulence in the daytime convective layer and wind shear in the stable nocturnal layer. Overall, the scanning lidar is a useful tool in observing the evolving boundary layer. The time–height cross sections provide a picture of the layer for a 32-h period. These cross sections are especially revealing during transition periods when the boundary layer dynamics are poorly understood. The scanning lidar should be useful in providing a more complete picture of these periods.

Acknowledgments. This material was based on the M.Sc. thesis in meteorology of one of the authors (WPH).

We gratefully acknowledge the field collection and analysis of the radiosonde data made by Douglas L.

[2] Data are compiled in Hooper (1982).

Sisterson of Argonne National Laboratory (ANL). The observations and analysis of data from kytoon and surface instruments made by Marvin L. Wesely, and his colleagues at ANL are also most gratefully acknowledged. The research at ANL was funded by the U.S. Environmental Protection Agency through interagency Agreement DW93006-01-0 to the U.S. Department of Energy. The research at the University of Wisconsin was supported by the U.S. Army Research Office Grants DAA-C29-76-C-0156 and DAA-G29-80-K-0700. We would like to express our appreciation to Reinout Boers for his comments and suggestions.

REFERENCES

Boers, R., E. W. Eloranta and R. L. Coulter, 1984: Lidar observations of mixed layer dynamics: Tests of parameterized entrainment models of mixed layer growth rate. *J. Climate Appl. Meteor.*, **23**, 247–266.

Businger, J. A., 1973: Turbulent transfer in the atmospheric surface layer, *Workshop on Micrometeorology*. D. A. Haugen, Ed., Amer. Meteor. Soc.

Caughey, S. J., J. C. Wyngaard and J. C. Kaimal, 1979: Turbulence in the evolving stable boundary layer. *J. Atmos. Sci.*, **36**, 1041–1052.

Clarke, R. H., 1970: Observational studies of the atmospheric boundary layer. *Quart. J. Roy. Meteor. Soc.*, **96**, 91–114.

Frenzen, P., and L. L. Prucha, 1973: The WHAT system: A new digitized radiosonde and double theodolite balloon tracking system for atmospheric boundary layer investigations. Argonne National Lab., NTIS CONF-731205-1. 5 pp.

Haugen, D. A., J. C. Kaimal, C. J. Readings and R. Rayment, 1975: A comparison of balloon-borne and tower-mounted instrumentation for probing the atmospheric boundary layer. *J. Appl. Meteor.*, **14**, 540–545.

Hooper, W. P., 1982: The diurnal evolution of the planetary boundary layer: Lidar observations above a flat homogeneous surface. M.S. thesis, University of Wisconsin, 160 pp.

Kaimal, J. C., and D. A. Haugen, 1977: An acoustic doppler sounder for measuring wind profiles in the lower boundary layer. *J. Appl. Meteor.*, **16**, 1298–1305.

——, and J. E. Gaynor, 1983: The Boulder Atmospheric Observatory, *J. Climate Appl. Meteor.*, **22**, 863–880.

Kunkel, K. E., E. W. Eloranta and J. A. Weinman, 1980: Remote determination of winds, turbulence spectra and energy dissipation rates in the boundary layer from lidar measurements, *J. Atmos. Sci.*, **37**, 978–985.

Sasano Y., H. Hirohara, T. Yamasaki, H. Shimizu, N. Takeuchi and T. Kawamura, 1982a: Horizontal wind vector determination from the displacement of aerosol distribution patterns observed by a scanning lidar. *J. Appl. Meteor.*, **21**, 1516–1523.

——, H. Shimizu and N. Takeuchi, 1982b: Convective Cell Structures revealed by Mie laser radar observations and image data processing. *Appl. Opt.*, **17**, 3166–3169.

Sroga, J. T., 1979: Remote measurements of boundary layer velocity parameters by monostatic lidar. M.S. thesis, University of Wisconsin, 115 pp.

——, E. W. Eloranta and T. Barber, 1980: Lidar measurements of wind velocity profile in the boundary layer. *J. Appl. Meteor.*, **19**, 598–605.